MMS observations of energetic oxygen ions at the duskside magnetopause during intense substorms

Chen Zeng[1,2], Suping Duan[1], Chi Wang[1,2], Lei Dai[1], Stephen Fuselier[3,4], James Burch[3], Roy Torbert[5], Barbara Giles[6], Christopher Russell[7]

[1]State Key Laboratory of Space Weather, National Space Science Center, Chinese Academy of Sciences, China.

[2]University of Chinese Academy of Sciences, China.

[3]Southwest Research Institute, San Antonio, Texas, USA.

[4]The University of Texas at San Antonio, San Antonio, Texas, USA.

[5]University of New Hampshire, Space Science Center, Durham, New Hampshire, USA.

[6]NASA, Goddard Space Flight Center, Greenbelt, MD, USA.

[7]University of California Los Angeles, IGPP/EPSS, Los Angeles, California, USA.

Corresponding author: Chi Wang (cw@spaceweather.ac.cn), Suping Duan(spduan@nssc.ac.cn)

Abstract

Energetic oxygen ions (1-40 keV) observed by the Magnetospheric Multiscale (MMS) satellites at the duskside magnetopause boundary layer during phase 1 are investigated. There are 57 duskside magnetopause crossing events during intense substorms (AE>500 nT) are identified. These 57 events of energetic O^+ at the duskside magnetopause include 26 events during the expansion phase and 31 events during the recovery phase of intense substorms. It is found that the O^+ density in the duskside magnetopause boundary layer during the recovery phase (0.081 cm^{-3}) is larger than that during the expansion phase (0.069 cm^{-3}). The 26 events of energetic O^+ ion at the duskside magnetopause during intense substorm expansion phase are all under the southward interplanetary magnetic field (IMF). There are only 7 events under northward IMF and they all occurred during the intense substorm recovery phase. The density of energetic O^+ at the duskside magnetopause ranges from 0.007 to 0.599 cm^{-3}. The maximum density of O^+ occurred during the intense substorm recovery phase and under southward IMF. When the IMF is southward, the O^+ density shows an exponential increase with the IMF B_z absolute value. Meanwhile, The O^+/H^+ density ratio shows an exponential growth with the IMF B_y. These results

31   agree with previous studies in the near-Earth magnetosphere during intense substorm. It is suggested that

32   O^+ abundance in the duskside magnetopause boundary layer has a close relation with O^+ variations in the

33   near-Earth magnetosphere during intense substorms.

34   **1 Introduction**

35   Single charged oxygen ions (O^+) in the magnetosphere are exclusively from the ionosphere. They

36   are an important element in the mass and energy transport in the magnetospheric dynamic process,

37   especially during the expansion phase and recovery phase of intense substorms (e.g., Daglis et al., 1991,

38   1996; Duan et al., 2017; Fok et al., 2006; Ohtani et al., 2011; Ono et al., 2009; Nosé et al., 2000; Yau et

39   al.,1997, 2012; Kronberg et al., 2014). Processes in the magnetotail due to substorm can result in auroral

40   electrojet activity. This activity is generally caused by field-aligned currents increase and reflected by

41   the AE index (Tang and Wang, 2018). Previous studies have found that the density and energy density

42   of O^+ significantly increase with AE index in the near-Earth magnetosphere during the intense substorm

43   (e.g., Lennartsson and Shelley, 1986; Daglis et al., 1991, 1994; Duan et al., 2017). Lennartsson and

44   Shelley (1986) proposed that oxygen ions with energies less than 17 keV/e could provide 50% of the

45   density in the plasma sheet during disturbed geomagnetic activity. They found the increase in the O^+

46   energy density was strongest around local midnight where O^+ became the most abundant ion at AE~1000

47   nT. In the near-Earth plasma sheet (NEPS), The O^+ energy density has an explosively increases with AE

48   index in the range of larger than 500 nT during the intense substorm expansion phase (Daglis et al., 1994).

49   Previous studies reported that the O^+ from the nightside auroral region could rapidly feed in the near-

50   Earth magnetosphere during substorm expansion phase (e.g., Daglis and Axford, 1996; Duan et al., 2017;

51   Yu et al., 2013). Otherwise, the solar wind dynamic pressure also influences the oxygen content of ion

52   outflow from the ionosphere. Using the Thermal Ion Dynamics Experiment (TIDE) on the Polar satellite.

53   Elliott et al., (2001) found both the O^+ density and parallel flux increased with the solar wind dynamic

54   pressure.

55   The O^+ outflowing from the ionosphere with low energy of eV are accelerated to about 500 eV at

56   the high altitude polar region (e. g., Yau and André, 1997). Then they are convected tailward into the

57   lobe and the plasma sheet boundary layer. After O^+ enter the NEPS of magnetotail, they can be energized

58   up to tens of keV during intense substorm dipolarizations(e.g., Birn et al., 2013; Duan et al., 2017;

59 Fok,et al., 2006; Nosé et al., 2000; Ono et al., 2009; Yau et al., 2012). The inductive electric field

60 associated with substorm dipolarization is very significant for accelerating particles in the NEPS (e.g.,

61 Dai et al., 2014, 2015; Duan et al., 2011, 2016; Lui et al., 1999). Duan et al. (2017) reported that the O^+

62 from the lobe or the plasma sheet boundary layer were efficiently accelerated by the kinetic Alfven

63 eigenmode with significant unipolar electric field and rapidly feed in the NEPS during intense substorm

64 dipolarizations. These energetic O^+ in the NEPS can be injected into the inner magnetosphere and drift

65 westward into the duskside outer magnetosphere (e.g., Ganushkina et al., 2005).

66   Oxygen ions decay from the ring current can leak into the dayside magnetopause boundary layer

67 (e.g., Li et al., 1993; Ebihara et al., 2011). Li et al. (1993) reported that the ring current O^+ with tens of

68 keV energy interacted with the Pc 5 waves and then lost towards the dayside magnetopause.The solar

69 wind dynamic pressure enhancement plays a key role in the ring current particle loss into the outer

70 magnetosphere. This pressure enhancement pushing the magnetopause to move inward leads to a

71 reduction of the scale length of the magnetic field magnitude gradient along the magnetopause. The

72 magnetic gradient drift speed across the magnetopause will increase. So the ring current oxygen ions

73 along the magnetic gradient drift path can easily enter into the outer magnetosphere (Kim et al., 2005).

74 Ebihara et al. (2011) proposed that the field line curvature scattering was more effective on the loss of

75 energetic oxygen ions with its large gyro-radius. The energetic oxygen ions with pitch angle of ~90

76 degrees are more prone to leak into the dayside magnetopause.

77   The distribution of energetic oxygen ions density at the dayside magnetopause is asymmetry and it

78 has a close relationship with the interplanetary magnetic field (IMF) (e.g., Bouhram et al., 2005; Phan et

79 al., 2004; Luo et al., 2017). Bouhram et al. (2005) pointed out that the O^+ density in the duskside (on

80 average 0.053 cm^{-3}) magnetopause is higher than that in the dawnside (on average 0.014 cm^{-3}). They

81 found O^+ was the dominant contributor to the mass density (30%) on the duskside magnetopause in

82 comparison to 3% in the dawnside and 4% near the noon. The dawn-dusk asymmetries of the energetic

83 O^+ (>~274 keV) distribution in three different regions (dayside magnetopause, near-Earth nightside

84 plasma sheet, and tail plasma sheet) are also observed by Luo et al., (2017). They found that the energetic

85 O^+ distributions were mainly influenced by the dawn-dusk IMF directions and the enhancement of ion

86 intensity strongly related to the location of the magnetopause reconnection.

87   There is ample evidence that magnetospheric ions could participate in the magnetopause

88 reconnection and directly escape along the reconnected open field lines (e.g., Sonnerup et al.,1981;

89 Fuselier et al., 1991, 2016; Slapak et al., 2012, 2015; Wang et al., 2014; Liu et al., 2015). The energetic

90 O^+ with energies larger than 3 keV in the reconnection jets at the duskside mid-latitude magnetopause

91 under steady southward IMF was reported by Phan et al. (2004). Zong et al., (2001) observed O^+ energy

92 dispersion due to time-of-flight (TOF) effects at the duskside magnetopause under southward IMF and

93 it was assumed that O^+ was escaping from the ring current along the reconnected field lines during steady

94 reconnection. However, Fuselier et al. (1989) reported that O^+ from the high latitude ionosphere were

95 not associated with any substorm cycle. O^+ from the high latitude ionosphere could form the O^+ rich

96 boundary layer in the low latitude magnetopause. When O^+ enter the reconnection jets, the reconnection

97 rate is likely reduced by the mass-loading but not suppressed at the magnetopause (Fuselier et al. 2019).

98   At present, variations of O^+ abundance (O^+/H^+) in the duskside magnetopause boundary layer

99 during intense substorm (AE >500 nT) on AE index and solar wind conditions (e.g. IMF B_y, IMF B_z and

100 solar wind dynamic pressure) are still not clear. Previous studies of O^+ abundance variations during

101 substorms are mainly focused on the magnetotail or the near-Earth region (e.g., Duan et al., 2017; Nosé

102 et al., 2000; Ohtani et al., 2011). The Magnetospheric Multiscale (MMS) mission gives us an opportunity

103 to focus on the O^+ in the duskside magnetopause region. In this study, we investigate statistical features

104 of energetic O^+ at the duskside magnetopause and their relations with AE index and solar wind conditions

105 (e.g. IMF B_y, IMF B_z, and solar wind dynamic pressure) during the intense substorms (AE >500 nT).

106 **2 Instrumentation and Data**

107   This study used data from the Magnetospheric Multiscale (MMS) mission. This mission comprises

108 four identical satellites that were launched on 2015 March 13 into an elliptical 28-inclination orbit with

109 perigee around 1.2 R_E and apogee around 12 R_E (Burch et al., 2016; Fuselier, et al., 2016b). The electric

110 field **E** is from the electric double probe (EDP) (Ergun et al., 2016; Lindqvist et al., 2016), and magnetic

111 field **B** is from the Fluxgate Magnetometer (FGM) (Russell et al., 2016). The plasma data are from the

112 Fast Plasma Investigation (FPI) and the Hot Plasma Composition Analyzer (HPCA). The FPI provides

113 plasma (electrons and ions) distribution functions at 32 energies from 10 eV to 30 keV. And it has a high

114 time resolution of 0.03 s for electrons and 0.15 s for ions in the burst mode and 4.5 s in the fast mode

115 (Pollock et al., 2016). The FPI does not discriminate between different ion species. While the HPCA

116 provides ion composition (H^+, He^{++}, He^+, and O^+) measurements in the energy range from 1 eV/q to 40

117 keV/q (Young et al., 2016). Although the HPCA instrument employs radio frequency (RF) unit to

118 artificially reduce the proton fluxes in some areas where the proton fluxes are intense, there still exists a

119 low level of background that affects the O^+ fluxes in the magnetosheath. The majority of the O^+ fluxes in

120 the magnetosphere side of the magnetopause are at energies from 1 keV to 40 keV and that band below

121 1keV visible in the magnetosheath side are observations outside the RF operating range and

122 contamination from high proton fluxes. Due to this contamination, the O^+ at energies from1 keV to 40

123 keV in the magnetopause boundary layer are considered in our study. The O^+ density recalculated from

124 the HPCA distribution functions at this energy range by using the Space Physics Environment Data

125 Analysis System (SPEDAS) software package. More details about SPEDAS can be found in

126 Angelopoulos et al. (2019). The solar wind parameters and AE index are available from the OMNI data

127 in CDAweb (http://cdaweb.gsfc.nasa.gov/). The data from the MMS 4 satellite are adopted in our

128 investigation since the data difference from other three spacecraft is negligible. This is due to spacecraft

129 separation and scales of particle motion.

130 **3 Results**

131 **3.1 Detailed event on 3 October 2015**

132   Figure 1 presents the three components of the IMF in Geocentric Solar Magnetospheric (GSM)

133 coordinates, solar wind dynamic pressure, as well as AU, AL, and AE index during the time of interest

134 from 14:30 to 16:30 UT on 3 October 2015. During this interval, the IMF B_x component is negative all

135 the time (Figure 1a). Its maximum value is about -1 nT at ~15:16 UT. The IMF B_y component is almost

136 negative except at ~14:32 and ~16:23 UT. The negative IMF B_z component is also observed during this

137 interval as shown in Figure 1c. The minimum value of the IMF B_z component is about -7.1 nT at ~14:30

138 UT. The solar wind dynamic pressure is only at the beginning of the time interval about 2 nPa. Then, it

139 increases sharply at 15:00 UT and reaches its maximum value about 4.4 nPa at ~15:12 UT. These solar

140 wind conditions led to an intense substorm (AE > 500 nT), as Figure 1g shown. The AE index is defined

141 as AE=AU-AL. Generally, the substorm onset time is characterized by the AL index starting to

142 significantly decrease and the AE index significantly increase. The interval of the AL index decreasing

143 from onset to its minimum is defined as the substorm expansion phase. The interval of the AL index

144 increasing from the minimum to the quiet time level is regarded as the substorm recovery phase. From

145 Figure 1e to 1g, the substorm onset time is about 14:45 UT marked by the AL index starting to sharply

146 decrease and AE index increase. After the AE index significantly increases and the AL index decreases

147 (Figure 1f), the AL and AE indexes reach their minimum and maximum values about -750 nT and 1000

148 nT at ~15:20 UT, respectively. This interval from ~14:45 to ~15:20 UT is regarded as the intense

149 substorm expansion phase. Then, the intense substorm enters the recovery phase as the AL index

150 gradually increases and AE index decreases after ~15:20 UT. The two blue dashed lines indicate the time

151 interval of the magnetopause boundary layer crossing. According to the above description, we can

152 identify this magnetopause boundary layer crossing occurred during the recovery phase of intense

153 substorm. The identification of the magnetopause boundary layer will be described later.

154 Figure 2 shows the overview of the magnetopause inbound crossing from 15:00 to 16:00 UT on 03

155 October 2015. During the magnetopause crossing, MMS 4 satellite was located at about (6.0, 8.8, -5.1)

156 R_E in GSM as shown in the bottom of Figure 2. From top to bottom, panels 2a and 2b show the magnetic

157 and electric fields in GSM from FGM and EDP, respectively. Ion and electron temperatures, plasma

158 density and ion velocity in GSM from FPI L2 data products are shown in Figures 2c-e. Figure 2f shows

159 the H^+ and O^+ densities, followed by the electron and ion omnidirectional differential energy fluxes from

160 FPI (Figure 2g-h). The last four panels present the differential fluxes of four individual ion species, H^+,

161 O^+, He^+, and He^{++} measured by HPCA, respectively. The HPCA flux in panels 2i-l has artificial striping

162 every 4 energy bins due to way HPCA determines the count rate over 4 energy channels in survey mode.

163 It is noted that the differential fluxes (Figure 2i-l) and differential energy fluxes (Figures 2g-h) have

164 different units. To better identify the fluxes variations at specific energies, we choose the ion and electron

165 fluxes from FPI in the energy flux unit. The plasma moments (e.g. ion parallel and perpendicular

166 temperatures, ion and electron densities, and ion velocity) from FPI shown in Figures 2c-e are all from

167 MMS L2 data products. They are default moments calculated over the full FPI energy range from 10 eV

168 to 30 keV. Note that in the magnetosheath, O^+ measurements suffer from fake counts at energies below

169 1 keV which results from high proton fluxes contamination, as the red box in Figure 2j shown. So the

170 spurious counts should be excluded in the plasma moments calculation. The O^+ density shown in Figure

171 2f is recalculated from HPCA distribution functions at energies from 1 keV to 40 keV. Due to H^+

172 measurements from HPCA is accurate and the H^+ mean energy in the magnetosheath is typically 0.3 keV,

173 we adopted the default H^+ density from HPCA L2 data products which computed over the full HPCA

174 energy range from 1 eV to 40 keV, as the red line shown in Figure 2f.

175   The different regions encountered by MMS4 during the interval of 15:00 to 16:00 UT are marked

176   by the colored bar at the top of Figure 2, with the magnetosheath shown in orange, the outer

177   magnetosphere shown in blue, and the magnetopause boundary layer shown in green. From 15:00:00 to

178   15:25:10 UT, MMS4 was located in the magnetosheath. This region is characterized by the southward

179   magnetic field, low ion and electron temperatures (a few hundred eV for ions and tens of eV for electrons,

180   Figure 2c) with relatively high densities (on the order of ~20 cm^{-3}, Figure 2d), and stable ion flow speed

181   of about 100 km/s. There are also very high fluxes at energies centered around 100 eV (nominal

182   magnetosheath energy) for electrons (Figure 2g) and at energies centered around 1 keV for ions (Figure

183   2h, also see H$^+$ fluxes in Figure 2i and He^{++} fluxes in Figure 2l) in the magnetosheath. While the O$^+$ and

184   He$^+$ fluxes above 1 keV nearly disappear in the magnetosheath (Figure 2j and 2k). From Figure 2j, the

185   majority of the O$^+$ fluxes at energies below 1 keV visible in the magnetosheath are the result of

186   contamination from the high proton fluxes, as the red box indicated.

187   The primary magnetopause crossing from the magnetosheath into the magnetosphere lasts about 12

188   min, from about 15:25:10 to 15:36:50 UT. Partial encounters of the magnetopause by MMS4 occurred

189   around 15:43:15, 15:47:10, 15:53:00 UT and etc. The magnetopause boundary layer is identified by the

190   plasma moments and the electromagnetic field. The plasma density and temperature at the magnetopause

191   are between the corresponding values of the magnetosphere and the magnetosheath, as shown in Figure

192   2d and 2c. The magnetopause boundary layer can also be identified by the significant increases in

193   electron fluxes at energies about several hundred eV and ion fluxes at energies around ~10 keV, as shown

194   in Figure 2g and 2h, respectively. During this time of interest, the B$_z$ component rotated from southward

195   to northward and back again several times before finally became northward when MMS 4 entered the

196   magnetosphere. The energetic O$^+$ density (1-40 keV) is around 0.018 cm^{-3} within the magnetopause

197   boundary layer as shown in Figure 2f. The corresponding H$^+$ and O$^+$ fluxes at specific energies and their

198   densities (shown in Figure 2f) were averaged in this region.

199   After 15:36:50 UT, MMS4 entered the magnetosphere which is identified by the observations of

200   the northward magnetic field (Figure 2a), much lower plasma densities (on the order of ~1 cm^{-3}) with

201   respect to the densities in the magnetosheath (Figure 2d), higher plasma temperatures (Figure 2c, several

202   keV for ions and a few hundred eV for electrons), and a small bulk ion flow speed. Higher fluxes at

203   energies around several keV for electrons (Figure 2g) and at energies centered around ~10 keV for ions

204   (Figure 2h) also indicate that the MMS4 was in the magnetosphere. Finally, the presence of O$^+$ and He$^+$

205 at energies about ~10 keV is also used as a marker to verify that MMS4 was in the magnetosphere (Figure

206 2j and 2k).

3.2 Statistical 57 events of energetic O^+ at the duskside magnetopause during intense substorms

208 Based on the in-situ measurements of the dayside magnetopause crossings by MMS satellites in

209 phase 1, we identified the duskside magnetopause crossing event (complete magnetopause crossing from

210 the magnetosheath to the magnetosphere, vice versa) from the summary plot in

211 https://lasp.colorado.edu/mms/sdc/public/plots/. Then we plotted the more detailed overview figure of

212 these events to identify the magnetopause boundary layer, as Figure 2 shown. Only events with AE index

213 larger than 500 nT during the magnetopause boundary layer crossings interval were selected. There are

214 57 events of the dusksideside magnetopause boundary layer crossing during intense substorm satisfied

215 with the above criterion. In our statistical study, the mean values of the H^+ and O^+ fluxes at specific

216 energies and their densities are calculated in the magnetopause boundary layer. Correspondingly, the

217 solar wind dynamic pressure, IMF B_y, B_z and AE index from the OMNI data system were averaged

218 during the magnetopause boundary layer crossing time interval, as the two blue dashed lines shown in

219 Figure 1. The phase of the substorm is determined from the variations of AU, AL and AE indexes, as

220 mentioned before. For better follow-on studies, we add more detail information about 57 energetic O^+

221 events into an appendix. From the appendix, we can easily draw the conclusion that the O^+ density in the

222 duskside magnetopause during the recovery phase (0.081 cm^{-3}) of intense substorm is larger than that

223 during the expansion phase (0.069 cm^{-3}).

224 Figure 3 displays the locations of 57 energetic O^+ events at the duskside magnetopause (-5.7 $R_E <$

225 $Z_{GSM} < 1.7$ R_E) during intense substorms projected into the XY_{GSM} plane. The blue curve line represents

226 the nominal magnetopause, which is obtained by the magnetopause model of Shue et al., (1998) when

227 the IMF B_z is about -3.21 nT and solar wind dynamic pressure (Psw) is ~2.87 nPa (averaged for the 57

228 events). The diamond and circle represent the event at the duskside magnetopause during the intense

229 substorm expansion phase and recovery phase, respectively. The O^+ density and the O^+/H^+ density ratio

230 are shown by the colored diamonds and circles at the corresponding magnetopause locations in Figures

231 3a and 3b, respectively. Among the 57 events of energetic O^+ at the duskside magnetopause during

232 intense substorms, there are 26 events that occurred during the expansion phase of intense substorms and

233   31 events occurred during the recovery phase. The maximum density of energetic O^+ is found during the

234   intense substorm recovery phase, as presented in Figure 3a.

235   Figure 4 presents the relationship between the energetic O^+ at the duskside magnetopause and AE

236   index during intense substorms. From top to bottom, panels show the O^+ and H^+ densities (Figure 4a),

237   the O^+/H^+ density ratio (Figure 4b) and O^+/H^+ particle fluxes ratios at different energy ranges (Figure 4c),

238   respectively. The energy channel ranges for O^+ and H^+ in the HPCA are the same. So the O^+/H^+ particle

239   fluxes ratio is directly defined as the ratio between mean values of their fluxes, respectively. The particle

240   fluxes are chosen at energies ~1 keV (energy range from 987.82 to 1165.21 eV), ~10 keV (energy range

241   from 9.97 to 11.77 keV), ~20 keV (energy range from 19.31 to 22.78 keV) and ~35 keV(energy range

242   from 31.69 to 37.39 keV). The error bars indicating the 90% confidence interval (CI) are also overplotted

243   in each point. The confidence interval is based on the following formula:

244
$$\bar{x} - k\frac{s}{\sqrt{n}} < \mu < \bar{x} + k\frac{s}{\sqrt{n}}$$

245   Where $\bar{x}$, s and n are the mean value, standard deviation and the sampling number of observations,

246   respectively. k in the above formula can be determined by calculating a 90% confidence interval for each

247   events (the k value is 1.65). Figure 4a shows that energetic O^+ density at the duskside magnetopause

248   during intense substorms is in the range from 0.007 to 0.599 cm^{-3}. The maximum density value of

249   energetic O^+ at the duskside magnetopause during intense substorm recovery phase is presented at the

250   higher AE index about 606 nT. The O^+/H^+ density ratio decreases with AE index from 900 to 1100 nT.

251   The variations of O^+ density and O^+/H^+ density ratio with AE index do not show obvious difference

252   between during the expansion phase and the recovery phase.

253   Figure 5 shows the relationship between the energetic O^+ at the duskside magnetopause and IMF

254   B_y during intense substorms. The format of Figure 5 is the same as that of Figure 4. Figure 5a shows that

255   the O^+ and H^+ densities decrease with IMF B_y from -6 to 0 nT and increase with IMF B_y from 4 to 8 nT.

256   From Figure 5b, the O^+/H^+density ratio shows an exponential growth with the IMF B_y. Based on the

257   scatter plot in Figure 5b, we can define linear functional dependence between the logarithm of O^+/H^+

258   density ratio and IMF B_y, as Eq. (1) shown. And the corresponding correlation coefficients is 94%. The

259   correlation coefficient close to 100% indicates that there is a great correlation.

260
$$\log\frac{n_{O^+}}{n_{H^+}} = 0.126 * \text{IMF By} - 5.174 \qquad\qquad (1)$$

261   The dependency is constructed using a linear least-squares fit unless otherwise stated. The O^+/H^+

262   particle flux ratio at energy ~10 keV, ~20 keV and ~35 keV also show an obvious exponential increase

263   with IMF B_y. This dependency is consistent with Welling et al. (2011) simulation results found in the

264   ring current.

265   Figure 6 shows the relationship between the energetic O^+ at the duskside magnetopause and IMF

266   B_z during intense substorms. The format of Figure 6 is the same as that of Figure 4. Figure 6a and 6b

267   both present that among 57 events of energetic O^+ at the duskside magnetopause boundary layer during

268   intense substorm, there are 50 events under southward IMF and only 7 events under northward IMF. It

269   is noted that 26 events occurred during the expansion phase of intense substorms which are all under the

270   southward IMF conditions, as the blue points shown. Meanwhile, the events that occurred under

271   northward IMF are all during the intense substorm recovery phase, as the right red points with positive

272   IMF B_z shown. From -10 to 0 nT, the O^+ density shows an obvious decrease with IMF B_z. To better

273   describe this variation trend, the empirical functional relation between the logarithm of O^+ density and

274   IMF B_z (from -10 to 0 nT) is established in Eq.(2) and the corresponding correlation coefficient is 94%.

275   While the O^+ density has a positive correlation with IMF B_z from 0 to 5 nT.

276    $$\log n_{O^+} = -0.163 * \text{IMF Bz} - 3.737 \qquad (2)$$

277   From Figure 6b, the O^+/H^+ density ratio during the recovery phase decrease with IMF B_z from about -2

278   to 2 nT. The maximum density of energetic O^+ at the duskside magnetopause is under southward IMF.

279   Meanwhile, the maximum O^+/H^+ density ratio at the duskside magnetopause is also under southward

280   IMF.

281   Figure 7 displays the relationship between the energetic O^+ at the duskside magnetopause and solar

282   wind dynamic pressure during intense substorms. The format of Figure 7 is the same as that of Figure 4.

283   Figure 7a presents that the O^+ density at the duskside magnetopause during intense substorms has a

284   positive correlation with the solar wind dynamic pressure. The empirical functional relation between the

285   logarithm of O^+ density and solar wind dynamic pressure (from 1 to 4.5 nPa) is also established in Eq.(3)

286   and the corresponding correlation coefficient is 94%.

287    $$\log n_{O^+} = 0.325 * \text{Psw} - 4.061 \qquad (3)$$

288   From Figure 7b, the O^+/H^+ density ratio during recovery phase show a decrease from about 2.5 to 3 nPa.

289   It is noted that the O^+/H^+ density ratio increase with solar wind dynamic pressure from about 3 to 4 nPa.

290   The maximum density of energetic O^+ at the duskside magnetopause, ~0.599 cm^{-3} take place at solar

291   wind dynamic pressure is about 3.9 nPa. While the maximum O^+/H^+ density ratio at the duskside

292   magnetopause appeared at solar wind dynamic pressure around 2.2 nPa. More details can be found in the

293   appendix.

294   **4 Discussion**

295   Energetic O^+ (1-40 keV) with high density are observed by MMS satellites at the duskside

296   magnetopause during the expansion phases and recovery phases of intense substorms, as displayed in

297   Figure 3a. The density of energetic O^+ is in range from 0.007 cm^{-3} to 0.599 cm^{-3} at the duskside

298   magnetopause boundary layer during intense substorms. In a companion paper from Zeng et al. (2019),

299   they study the O^+ abundance variations on the solar wind conditions at the dayside magnetopause

300   boundary layer and not specific to the events that occurred during intense substorm. The mean value of

301   the O^+ density at the duskside magnetopause boundary layer is 0.038 cm^{-3} in that paper. While during the

302   intense substorm, the O^+ density increase to 0.075 cm^{-3} in this study. There are two reasons for this high

303   density of energetic O^+ observed during the intense substorm. The first is the time interval for the

304   observations. Our observations are during intense substorms expansion phase and recovery phase. Daglis

305   et al. (1991) proposed that energetic O^+ were significantly higher in the NEPS in the magnetotail after

306   intense substorms onset. The impulsive electric field accompanied by intense substorm dipolarization

307   plays a key role in the energization and sunward transfer of oxygen ions in the duskside of midnight

308   plasma sheet in the magnetotail (e.g., Fok et al., 2006; Nosé et al., 2000). These energetic O^+ (tens of

309   keV) can be transported sunward into the duskside magnetopause boundary layer. The second reason for

310   the high densities is the locations of the observations. Our observations are near the duskside

311   magnetopause. This region is easily accessible by energetic O^+ during intense geomagnetic activity

312   (Fuselier et al. 2016a). Phan et al. (2004) pointed out that energetic O^+ with very high density 0.2-0.3

313   cm^{-3} in the reconnection jets at the duskside mid-latitude magnetopause were observed by Cluster.

314   During dynamic periods and intense substorms time, light ions yielded more symmetric patterns in

315   density than heavy ions and the O^+ patterns in the active plasma sheet are a function of IMF conditions

316   (Winglee and Harnett 2011. Winglee et al. 2005). Welling et al. (2011) used multispecies MHD and the

317   PWOM to drive a ring current model and found that positive IMF B_y pushed the stronger O^+

318   concentrations toward the duskside at a geocentric distance of about 6.6 R_E. This O^+ density duskward

319   preference with positive IMF B_y in the NEPS is similar to our results. It may indicate that O^+ in the

320   magnetopause boundary layer enhancing with IMF B_y is due to the local time variations of O^+ in the

321   NEPS tied to IMF B_y. Our result of O^+ density increase with IMF B_y also agree with Kronberg et al.,

322   (2012). They showed for 10 keV O^+ strong increasing under the duskward IMF indicated by the clock

323   angle in the inner magnetosphere. It is suggested that the O^+ abundance at the duskside magnetopause

324   has a corresponding relation with the O^+ in the duskside near-Earth magnetosphere during intense

325   substorm. The O^+ path from the cusp to the magnetotail is asymmetry and it has the best correlation with

326   the IMF directions. This path asymmetry mainly controlled by the IMF B_y may influence on O^+

327   abundance at the duskside magnetopause. When the IMF B_y is positive, the O^+ from northern/southern

328   cusp tends to flow toward the dawnside/duskside. The transport path for negative IMF B_y is more

329   symmetric but shows some evidence for a reversed asymmetry when the negative IMF B_y is large enough.

330   While the IMF B_z has little influence on the asymmetry (Liao et al., 2010).

331   Due to not enough events occurred under northward IMF were observed, the influence of IMF B_z

332   on the O^+ abundance (1-40 keV) during intense substorm is not clear. While in Luo et al. (2017) study

333   that not only the cases for the intense substorm were considered, they found the O^+ intensity (> ~274 keV)

334   was significantly higher under southward IMF than that under northward IMF especially at the duskside

335   magnetopause. Zeng et al. (2019) also showed that the duskside asymmetry of O^+ density (1-40 keV) in

336   the dayside magnetopause under northward IMF was less obvious than under southward IMF when the

337   IMF B_y was the same. Under the southward IMF, the interactions between the solar wind and the

338   magnetosphere become active. The inductive electric field or magnetic field gradient related to magnetic

339   reconfiguration will enhance with negative IMF B_z. So the large scale dawn-dusk electric field drift along

340   with the gradient-curvature drift can force oxygen ions convect to the duskside magnetopause boundary

341   layer (Kronberg et al., 2015; Luo et al., 2017).

342   In this statistical study, there are 50 magnetopause boundary layer crossing events during intense

343   substorm under southward IMF with respect to 7 events under northward IMF. Choosing the intense

344   substorm may increase the probability of observing the events under southward IMF quite significantly.

345   Among 57 events of energetic O^+ near the duskside magnetopause, there are 26 events during intense

346   substorm expansion phase which are all under the southward IMF, as the blue circle shown in Figure

347   6b.There are only 7 events under northward IMF in our study and they all occurred during the intense

348 substorm recovery phase. But what relation between the IMF directions and phase of substorm is out of

349 scope for this article.

350   Previous researches demonstrated that the oxygen ions origin from the aurora region could rapidly

351 feed in the NEPS during intense substorms expansion phase (e.g., Daglis and Axford, 1996; Duan et al.,

352 2017; Yu et al., 2013). Oxygen ions can be efficiently energized in the NEPS during intense substorm

353 dipolarization (e.g., Duan et al., 2017; Fok et al., 2006; Nosé et al., 2000). Under southward IMF

354 conditions, these energetic oxygen ions in the NEPS can be convected sunward and drift westward. As a

355 result, the energetic O^+ arrived near the duskside magnetopause can participate in the magnetopause

356 reconnection and escape along reconnected field lines during intense substorm expansion phase, as

357 reported by Wang et al. (2014) and Zong et al. (2001). When O^+ participate in the reconnection jets, the

358 reconnection rate will likely be reduced by the mass-loading but not suppressed at the magnetopause

359 (Fuselier et al. 2019). Whether these energetic O^+ at the duskside boundary layer could suppress the

360 intense substorm need further investigation.

361 **5 Summary and conclusions**

362   Using the measurements from MMS satellite during the phase 1, we have studied 57 events of the

363 energetic O^+ (1-40 keV) at the duskside magnetopause boundary layer and their variations on the solar

364 wind conditions (IMF B_y, IMF B_z and solar wind dynamic pressure) during intense substorm expansion

365 phases and recovery phases. According to the above analysis, we can draw our main conclusions as

366 follows. In our 57 events of energetic O^+ at the duskside magnetopause boundary layer, there are 26

367 events during the expansion phase of intense substorms and 31 events during the recovery phase. It is

368 noted that the mean values of the O^+ density during the expansion phase and recovery phases are 0.069

369 cm^{-3} and 0.081 cm^{-3}, respectively. And the maximum O^+/H^+ density ratio occurred during the intense

370 substorm recovery phase. It is found that 26 events of energetic O^+ at the duskside magnetopause during

371 intense substorms expansion phase are all under the southward IMF conditions, and only 7 events under

372 northward IMF which are all during the intense substorm recovery phase. The O^+ density shows an

373 exponential increase with IMF B_z absolute value under the southward IMF. Similarly, it also presents an

374 exponential growth with solar wind dynamic pressure, and the empirical functional relations are

375 established. Like previous studies during substorm in the near-Earth magnetosphere, The O^+/H^+ density

376 ratio in the duskside magnetopause boundary layer enhance with the IMF B_y. It is suggested that the O^+

377 abundance in the duskside magnetopause boundary layer has a close correlation with the O^+ variations

378 in the near-Earth magnetosphere during intense substorm.

Data availability

380 All data used in this study are publicly accessible. MMS data are available at the MMS Science

381 Data Center (https://lasp.colorado.edu/mms/sdc/public/). The OMNI data can be downloaded from the

382 NASA Goddard Space Flight Center Coordinated Data Analysis Web

383 (CDAWeb:http://cdaweb.gsfc.nasa.gov/).

Competing interests

385 The authors declare that they have no conflict of interest.

Author contribution

387 C. Z. conducted the majority of the data processing, analysis and writing for this study. S.P.D, C.W,

388 L.D and S.F participated in the interpretation of the data and modified this paper. J.B, R.T, B.G and C.R

389 produced the data and controlled the data quality. All the authors discussed the results and commented

390 on the paper.

Acknowledgments

392 We acknowledge the entire MMS team for providing high-quality data. This work is supported by

393 the National Natural Science Foundation of China grants 41874196, 41674167; 41731070, 41574161

394 and 41574159; the Strategic Pioneer Program on Space Science, Chinese Academy of Sciences, grants

395 XDA15052500, XDA15350201 and XDA15011401; the NSSC Research Fund for Key Development

396 Directions and in part by the Specialized Research Fund for State Key Laboratories.

References

398 Angelopoulos, V., Cruce, P., Drozdov, A. et al. (2019), The Space Physics Environment Data Analysis
399 System (SPEDAS), Space Sci Rev., 215(9), doi:10.1007/s11214-018-0576-4.

Birn, J., Thomsen, M. F., and Borovsky, J. E. et al.: Substorm ion injections: Geosynchronous observations and test particle orbits in three-dimensional dynamic MHD fields, J. Geophys. Res., 102, 2325–2341, 1997.

Bouhram, M., Klecker, B., Paschmann, G., Haaland, S., Hasegawa, H., Blagau, A., et al. (2005). Survey of energetic O^+ ions near the dayside mid-latitude magnetopause with Cluster. Annales Geophysicae, 23(4), 1281–1294. doi:10.5194/angeo-23-1281-2005.

Burch, J. L., Moore, T. E., Torbert, R. B., and Giles, B. L. (2016). Magnetospheric Multiscale Overview and Science Objectives. Space Science Reviews, 199(1–4), 5–21. doi:10.1007/s11214-015-0164-9.

Daglis, I. A., N. P. Paschalidis, E. T. Sarris, W. I. Axford, G. Kremser, B. Wilken, and G. Gloeckler (1991), Statistical features of the substorm expansion phase as observed by AMPTE/CCE spacecraft, in Magnetospheric Substorms, Geophys. Monogr. Ser, vol. 64, edited by J. R. Kan et al., pp. 323–332, AGU, Washington, D. C.

Daglis, I. A., Livi, S., Sarris, E. T., and Wilken, B. (1994), Energy density of ionospheric and solar wind origin ions in the near‐Earth magnetotail during substorms, J. Geophys. Res., 99(A4), 5691–5703, doi:10.1029/93JA02772.

Daglis, I. A., and Axford, W. I. (1996). Fast ionospheric response to enhanced activity in geospace: Ion feeding of the inner magnetotail. Journal of Geophysical Research, 101(A3), 5047–5065, doi:10.1029/95JA02592.

Dai, L., J. R. Wygant, C. A. Cattell, S. Thaller, K. Kersten, A. Breneman, X. Tang, R. H. Friedel, S. G. Claudepierre, and X. Tao (2014), Evidence for injection of relativistic electrons into the Earth's outer radiation belt via intense substorm electric fields, Geophys. Res. Lett., 41, 1133–1141,doi:10.1002/2014GL059228.

Dai, L., Wang, C., Duan, S., He, Z., Wygant, J. R., Cattell, C. A.,…Tang, X. (2015). Near-Earth injection of MeV electrons associated with intense dipolarization electric fields: Van Allen Probes observations. Geophysical Research Letters, 42, 6170–6179. https://doi.org/10.1002/2015GL064955.

Duan, S. P., Liu, Z. X., Liang, J., Zhang, Y. C., and Chen, T. (2011). Multiple magnetic dipolarizations observed by THEMIS during a substorm. Annales de Geophysique, 29(2), 331–339, doi:10.5194/angeo- 29- 331- 2011.

Duan, S. P., L. Dai, C. Wang, J. Liang, A. T. Y. Lui, L. J. Chen, Z. H. He, Y. C. Zhang, and V. Angelopoulos (2016), Evidence of kinetic Alfvén eigenmode in the near-Earth magnetotail during substorm expansion phase, J. Geophys. Res. Space Physics, 121, 4316–4330, doi:10.1002/ 2016JA022431.

Duan, S., Dai, L., Wang, C., He, Z., Cai, C., Zhang, Y. C., … Khotyaintsev, Y. V. (2017). Oxygen ions O^+ energized by kinetic Alfvén eigenmode during dipolarizations of intense substorms. Journal of Geophysical Research: Space Physics, 122. https://doi.org/10.1002/ 2017JA024418

Ebihara, Y., M.‐C. Fok, T. J. Immel, and P. C. Brandt (2011), Rapid decay of storm time ring current due to pitch angle scattering in curved field line, J. Geophys. Res., 116, A03218, doi:10.1029/2010JA016000.

Elliott, H. A., Comfort, R. H., Craven, P. D., Chandler, M. O., and Moore, T. E. (2001), Solar wind influence on the oxygen content of ion outflow in the high‐altitude polar cap during solar minimum conditions, J. Geophys. Res., 106(A4), 6067–6084, doi:10.1029/2000JA003022.

Ergun, R. E., Tucker, S., Westfall, J., Goodrich, K. A., Malaspina, D. M., Summers, D., et al. (2016). The Axial Double Probe and Fields Signal Processing for the MMS Mission. Space Science Reviews, 199(1–4), 167–188. doi:10.1007/s11214-014-0115-x.

Fok, M., Moore, T. E., Brandt, P. C., Delcourt, D. C., Slinker, S. P., and Fedder, J. A. (2006). Impulsive enhancements of oxygen ions during substorms. Journal of Geophysical Research, 111, A10222, doi:10.1029/2006JA011839.

Fuselier, S. A., Klumpar, D. M., Peterson, W. K., and Shelley, E. G. (1989), Direct injection of ionospheric O^+ into the dayside low latitude boundary layer. Geophysical Research Letters, 16(10), 1121–1124. doi.:10.1029/GL016i010p01121.

Fuselier, S. A., D. M. Klumpar, and E. G. Shelley (1991), Ion reflection and transmission during reconnection at the Earth's subsolar magnetopause, Geophys. Res. Lett., 18, 139–142, doi:10.1029/90GL02676.

Fuselier, S. A., et al. (2016a), Magnetospheric ion influence on magnetic reconnection at the duskside magnetopause, Geophys. Res. Lett., 43,1435–1442, doi:10.1002/2015GL067358.

Fuselier, S. A., Lewis, W. S., Schiff, C., Ergun, R., Burch, J. L., Petrinec, S. M., and Trattner, K. J. (2016b). Magnetospheric Multiscale Science Mission Profile and Operations. Space Science Reviews, 199(1–4), 77–103. doi:10.1007/s11214-014-0087-x.

Fuselier, S. A., Trattner, K. J., Petrinec, S. M., Denton, M. H., Toledo‐Redondo, S., André, M., et al. (2019).Mass loading the Earth's dayside magnetopause boundary layer and its effect on magnetic reconnection. Geophysical Research Letters, 46, doi:10.1029/2019GL082384.

Ganushkina, N. Y., Pulkkinen, T. I., and Fritz, T. (2005). Role of substorm-associated impulsive electric fields in the ring current development during storms. Annales Geophysicae, 23(2), 579–591, doi:10.5194/angeo-23-579-2005.

Kim, K. C., Lee, D.‐Y., Lee, E. S., Choi, C. R., Kim, K. H., Moon, Y. J., Cho, K. S., Park, Y. D., and Han, W. Y. (2005), A new perspective on the role of the solar wind dynamic pressure in the ring current particle loss through the magnetopause, J. Geophys. Res., 110, A09223, doi:10.1029/2005JA011097.

Kronberg, E. A., Haaland, S. E., Daly, P. W., Grigorenko, E. E., Kistler, L. M., Fränz, M., and Dandouras, I. (2012), Oxygen and hydrogen ion abundance in the near-Earth magnetosphere: Statistical results on the response to the geomagnetic and solar wind activity conditions, J. Geophys. Res., 117, A12208, doi:10.1029/2012JA018071.

Kronberg, E. A., Ashour-Abdalla, M., Dandouras, I., Delcourt, D. C., Grigorenko, E. E., Kistler, L. M.,…Zelenyi, L. M. (2014). Circulation of heavy ions and their dynamical effects in the magnetosphere: Recent observations and models. Space Science Reviews, 184(1-4), 173–235, doi:10.1007/s11214-014-0104-0.

Kronberg, E. A., E. E. Grigorenko, S. E. Haaland, P. W. Daly, D. C. Delcourt, H. Luo, L. M. Kistler, and I. Dandouras (2015), Distribution of energetic oxygen and hydrogen in the near-Earth

480   plasma sheet, J. Geophys. Res. Space Physics, 120, 3415–3431, 681
481   doi:10.1002/2014JA020882.

482   Lennartsson, W., and Shelley, E. G. (1986). Survey of 0.1- to 16-keV/ e plasma sheet ion composition.
483   Journal of Geophysical Research, 91(A3), 3061.

484   Li, X., M. Hudson, A. Chan, and I. Roth (1993), Loss of ring current O^+ ions due to interaction with Pc
485   5 waves, J. Geophys. Res., 98, 215–231, doi:10.1029/92JA01540.

486   Liao, J., Kistler, L. M., Mouikis, C. G., Klecker, B., Dandouras, I., and Zhang, J.‐
487   C. (2010), Statistical study of O^+ transport from the cusp to the lobes with Cluster CODIF
488   data, J. Geophys. Res., 115, A00J15, doi:10.1029/2010JA015613.

489   Liu, Y. H., C. G. Mouikis, L. M. Kistler, S. Wang, V. Roytershteyn, and H. Karimabadi (2015),The
490   heavy ion diffusion region in magnetic reconnection in the Earth's magnetotail, J.Geophys.
491   Res., 120, 3535-3551, doi:10.1002/2015JA020982.

492   Lindqvist, P.-A., Olsson, G., Torbert, R. B., King, B., Granoff, M., Rau, D., et al. (2016). The Spin-
493   Plane Double Probe Electric Field Instrument for MMS. Space Science Reviews, 199(1–4),
494   137–165. doi:10.1007/s11214-014-0116-9.

495   Lui, A. T. Y., Liou, K., Nosé, M., Ohtani, S., Williams, D. J., Mukai, T., et al. (1999). Near-Earth
496   dipolarization: Evidence for a non-MHD process. Geophysical Research Letters, 26(19),
497   2905–2908. Doi:10.1029/1999GL003620.

498   Luo, H., E. A. Kronberg, K. Nykyri, K. J. Trattner, P. W. Daly, G. X. Chen, A. M. Du, and Y. S. Ge
499   (2017), IMF dependence of energetic oxygen and hydrogen ion distributions in the near-Earth
500   magnetosphere, J. Geophys. Res. Space Physics, 122, 5168–5180,
501   doi:10.1002/2016JA023471.

502   Nosé, M., Lui, A. T. Y., Ohtani, S., Mauk, B. H., McEntire, R. W., Williams, D. J.,…Yumoto, K.
503   (2000). Acceleration of oxygen ions of ionospheric origin in the near-Earth magnetotail during
504   substorms. Journal of Geophysical Research, 105(A4), 7669–7677,
505   doi:10.1029/1999JA000318.

506   Ohtani, S., M. Nosé, S. P. Christon, and A. T. Y. Lui (2011), Energetic O^+ and H^+ ions in the plasma
507   sheet: Implications for the transport of ionospheric ions, J. Geophys. Res., 116, A10211,
508   doi:10.1029/2011JA016532.

509   Ono, Y., M. Nosé, S. P. Christon, and A. T. Y. Lui (2009), The role of magnetic field fluctuations in
510   nonadiabatic acceleration of ions during dipolarization, J. Geophys. Res., 114, A05209,
511   doi:10.1029/2008JA013918.

512   Phan, T. D., Dunlop, M. W., Paschmann, G. et al.: Cluster observations of continuous reconnection at
513   the magnetopause under steady interplanetary magnetic field conditions, Ann. Geophys., 22,
514   2355–2367, 2004,

515   Pollock, C., Moore, T., Jacques, A., Burch, J., Gliese, U., Saito, Y., et al. (2016). Fast Plasma
516   Investigation for Magnetospheric Multiscale. Space Science Reviews, 199(1–4), 331–406.
517   doi:10.1007/s11214-016-0245-4.

518   Russell, C. T., Anderson, B. J., Baumjohann, W., Bromund, K. R., Dearborn, D., Fischer, D., et al.
519   (2016). The Magnetospheric Multiscale Magnetometers. Space Science Reviews, 199(1–4),
520   189–256. doi:10.1007/s11214-014-0057-3.

521   Shue, J. ‐ H., et al. (1998), Magnetopause location under extreme solar wind conditions, J. Geophys.
522   Res.,103(A8), 17691– 17700, doi:10.1029/98JA01103.

523   Sonnerrup, B. U. Ö., G. Paschmann, I. Papamastorakis, N. Sckopke, G. Haerendel, S. J. Bame, J. R.
524   Asbridge, J. T. Gosling, and C. T. Russell (1981), Evidence for magnetic field reconnection at
525   the Earth's magnetopause, J. Geophys. Res., 86, 10,049–10,067,
526   doi:10.1029/JA086iA12p10049.

527   Slapak, R., H. Nilsson, L. G. Westerberg, and A. Eriksson (2012), Observations of oxygen ions in the
528   dayside magnetosheath associated with southward IMF, J. Geophys. Res., 117, A07218,
529   doi:10.1029/2012JA017754.

530   Slapak, R., Nilsson, H., Westerberg, L. G., and Larsson, R (2015), O^+ transport in the dayside
531   magnetosheath and its dependence on the IMF direction, Ann. Geophys., 33, 301-307,
532   doi:10.5194/angeo-33-301-2015.

533   Tang, B., and Wang, C. (2018). Large scale current systems developed from substorm onset: Global
534   MHD results. Science China Technological Sciences, 61(3), 389–396, doi:10.1007/s11431-
535   017-9132-y.

536   Wang, S., L. M. Kistler, C. G.Mouikis, Y. Liu, and K. J. Genestreti (2014), Hot magnetospheric O^+ and
537   cold ion behavior in magnetopause reconnection: Cluster observations, J. Geophys.Res., 119,
538   9601-9623, doi:10.1002/2014JA020402.

539   Welling, D. T., Jordanova, V. K., Zaharia, S. G., Glocer, A., and Toth, G. (2011), The effects of
540   dynamic ionospheric outflow on the ring current, J. Geophys. Res., 116, A00J19,
541   doi:10.1029/2010JA015642.

542   Winglee, R. M., Lewis, W., and Lu, G. (2005), Mapping of the heavy ion outflows as seen by IMAGE
543   and multifluid global modeling for the 17 April 2002 storm, J. Geophys. Res., 110, A12S24,
544   doi:10.1029/2004JA010909.

545   Winglee, R. M., and Harnett, E. (2011), Influence of heavy ionospheric ions on substorm onset, J.
546   Geophys. Res., 116, A11212, doi:10.1029/2011JA016447.

547   Yau, A. W., and M. André (1997), Sources of ion outflow in the high latitude ionosphere, Space Sci.
548   Rev., 80, 1.

549   Yau, A. W., A. Howarth, W. K. Peterson, and T. Abe (2012), Transport of thermal-energy ionospheric
550   oxygen (O^+) ions between the ionosphere and the plasma sheet and ring current at quiet times
551   preceding magnetic storms, J. Geophys. Res., 117, A07215, doi:10.1029/2012JA017803.

552   Yu, Y., and A. J. Ridley (2013), Exploring the influence of ionospheric O^+ outflow on magnetospheric
553   dynamics: dependence on the source location, J. Geophys. Res. Space Physics, 118, 1711–
554   1722, doi:10.1029/2012JA018411.

555   Young, D. T., Burch, J. L., Gomez, R. G., De Los Santos, A., Miller, G. P., Wilson, P., et al. (2016).
556   Hot Plasma Composition Analyzer for the Magnetospheric Multiscale Mission. Space Science
557   Reviews, 199(1–4), 407–470. doi:10.1007/s11214-014-0119-6.

558   Zeng, C., Duan, S., Wang, C., Dai, L., Fuselier, S., et al. (2019). Statistical study of oxygen ions
559   abundance and spatial distribution in the dayside magnetopause boundary layer: MMS
560   observations, J. Geophys. Res. Space Physics, under review.

561   Zong, Q.‐G., Wilken, B., Fu, S. Y., Fritz, T. A., Korth, A., Hasebe, N., Williams, D. J., and Pu, Z.‐
562   Y. (2001),Ring current oxygen ions escaping into the magnetosheath, J. Geophys.
563   Res., 106(A11), 25541– 25556, doi:10.1029/2000JA000127.

 Figures and Captions
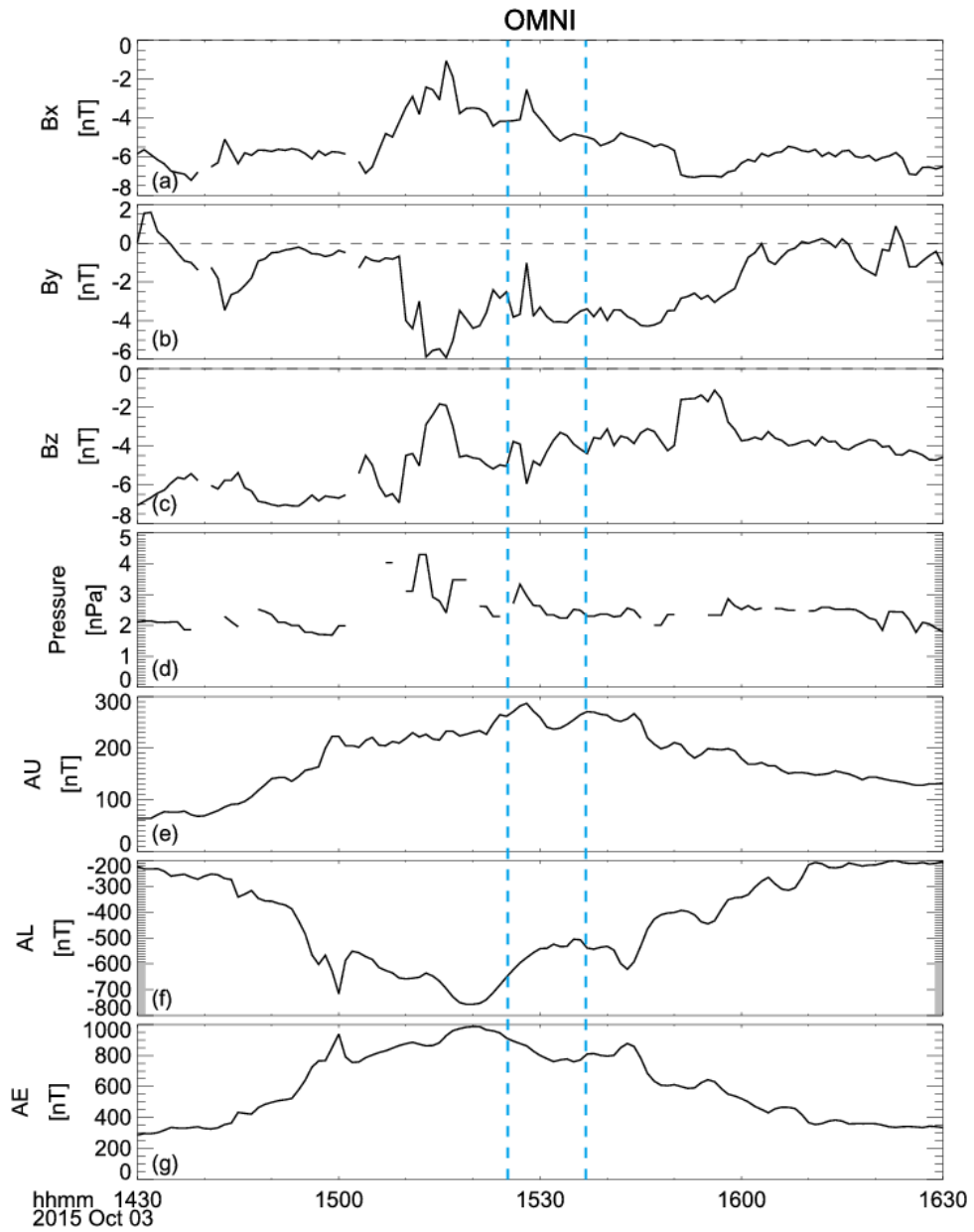
565

566 **Figure 1.** The three components of the IMF Bx, By, Bz in the Geocentric Solar Magnetospheric
567 coordinates, solar wind dynamic pressure, as well as AU, AL and AE index from CDAweb OMNI data.
568 The two blue dashed lines indicate the interval of the magnetopause boundary layer crossing.

569

570
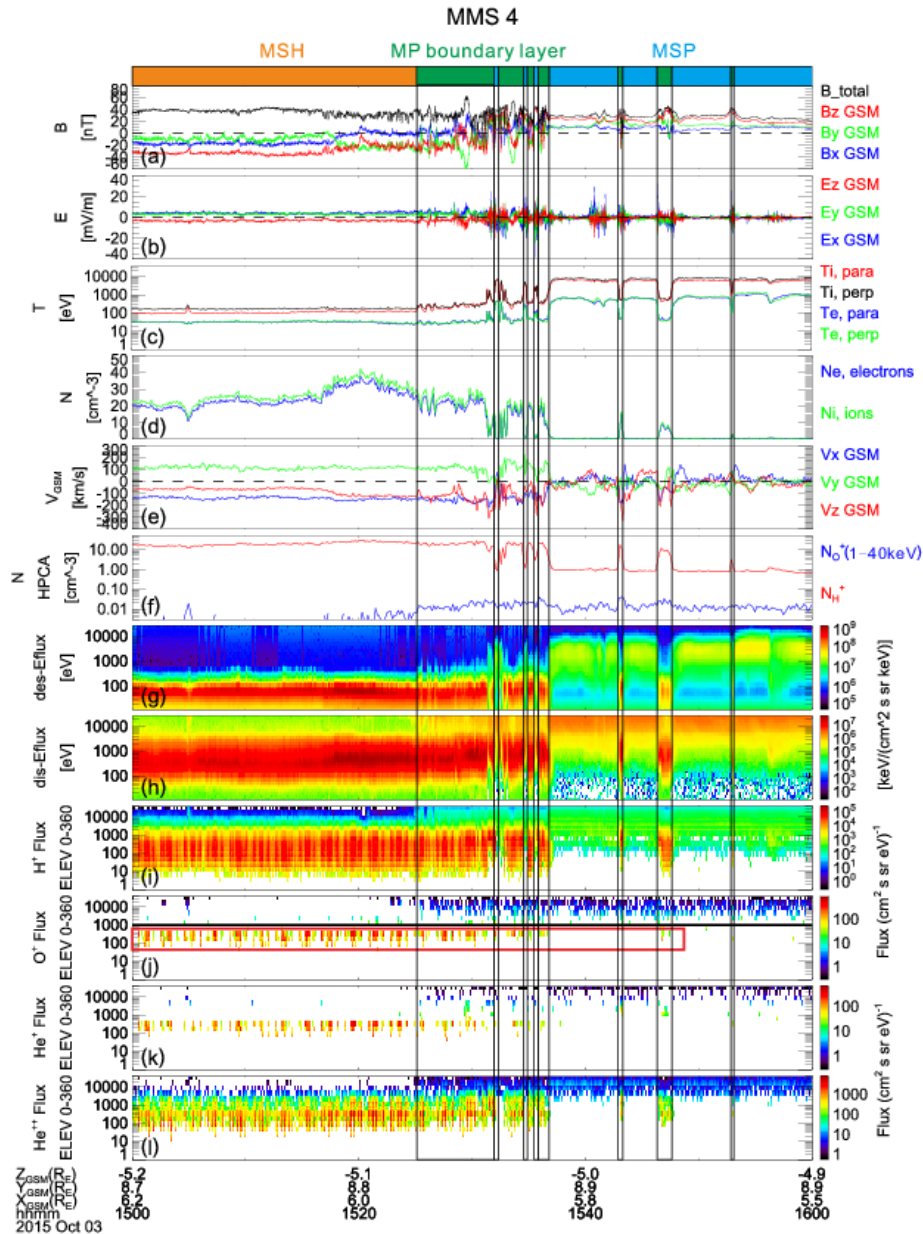
Figure 2. The energetic O^+ is observed at the magnetopause during an intense substorm on 03 October 2015 by MMS 4. From top to bottom are (a) the magnetic field three components, Bx (blue line), By (gree line), Bz (red line) and the total magnitude Bt (black line), (b) the electric field three components, Ex (blue), Ey (gree) and Ez (red), (c) ion parallel (red) and perpendicular (black) temperatures, as well as electron parallel (blue) and perpendicular (green) temperatures, (d) The density of ion (green) and electron (blue), (e) three components of the ion velocity, (f) the H^+ (over the full HPCA energy range from 1 eV to 40 keV) and O^+ (at energies from 1 keV to 40 keV) densities, (g-h) electron and ion omnidirectional differential energy fluxes (keV/(cm^2 s sr KeV)$^{-1}$), (i) to (l) present differential particle fluxes (cm^2 s sr eV)$^{-1}$ of H^+, O^+, He^+, He^{++}, respectively. The Geocentric Solar Magnetospheric coordinate system is adopted. The thick bars at the top of the panel present different regions encountered on this magnetopause crossing event. The orange and blue bars represent the magnetosheath and the magnetosphere, respectively. The green bar represents the magnetopause boundary layer. The black

583 horizontal line in figure 2j is at 1 keV and the O⁺ contamination from high H⁺ fluxes is indicated by the

584 red box. The FPI data in Figure 2c-e and g-h are from FPI L2 data products and in the fast mode.

585

586
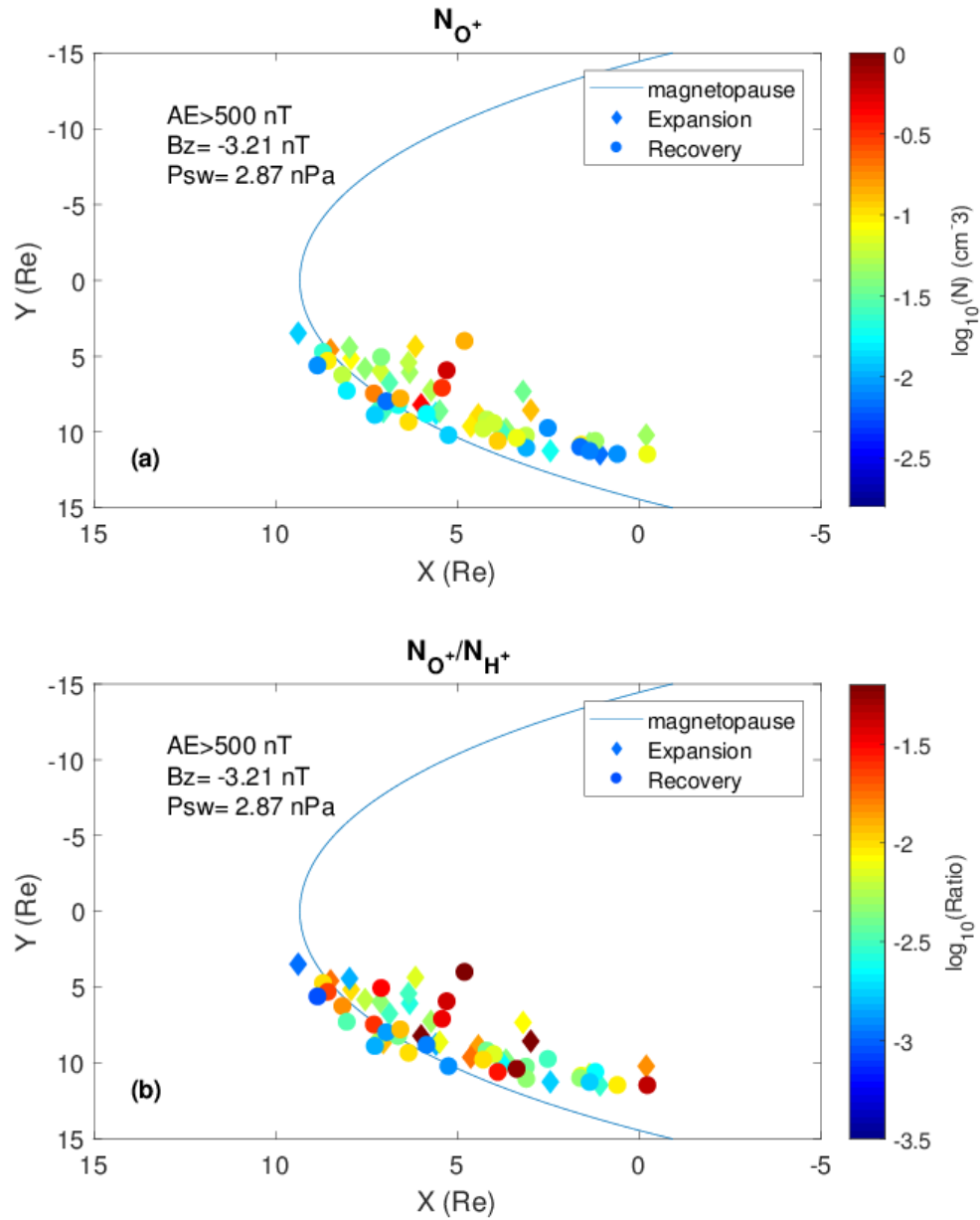
Figure 3. Maps of 31 events of energetic O⁺ at the duskside magnetopause during intense substorms with
AE index larger than 500 nT in XY_{GSM} plane. The O⁺ density and the density ratio of O⁺/H⁺ are shown
by the color signatures at the corresponding magnetopause location in Figure 3a and 3b, respectively.

 The blue curve line represents the nominal magnetopause. The diamond and circle represent the event at
591 the magnetopause during the intense substorm expansion phase and recovery phase, respectively.

592
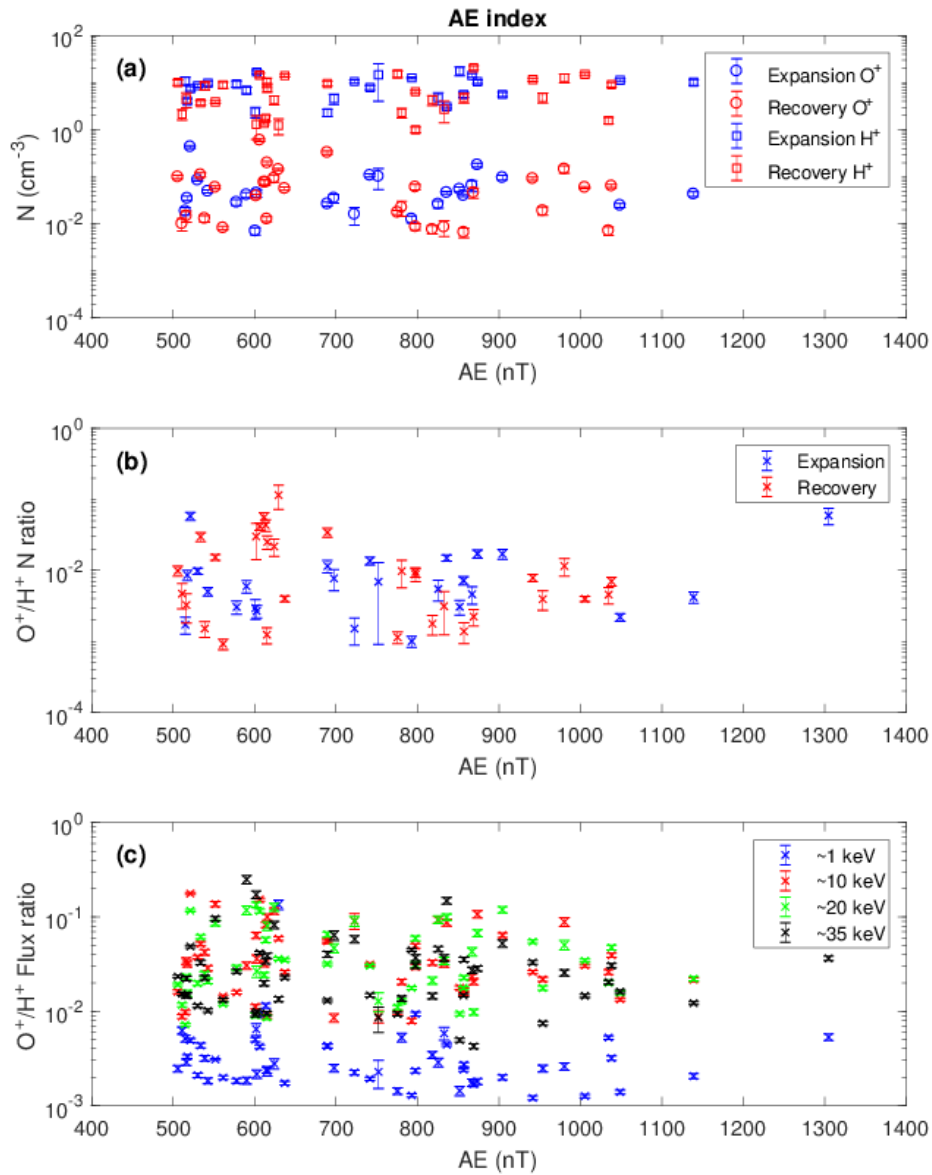
Figure 4. The relationship between the energetic O^+ at the duskside magnetopause and AE index during
intense substorms. From top to bottom, panels show the O^+ and H^+ densities (Figure 4a), the O^+/H^+
density ratio (Figure 4b), and the O^+/H^+ particle flux ratio (Figure 4c), respectively. Error bars indicate
90% confidence intervals.

597

598

599
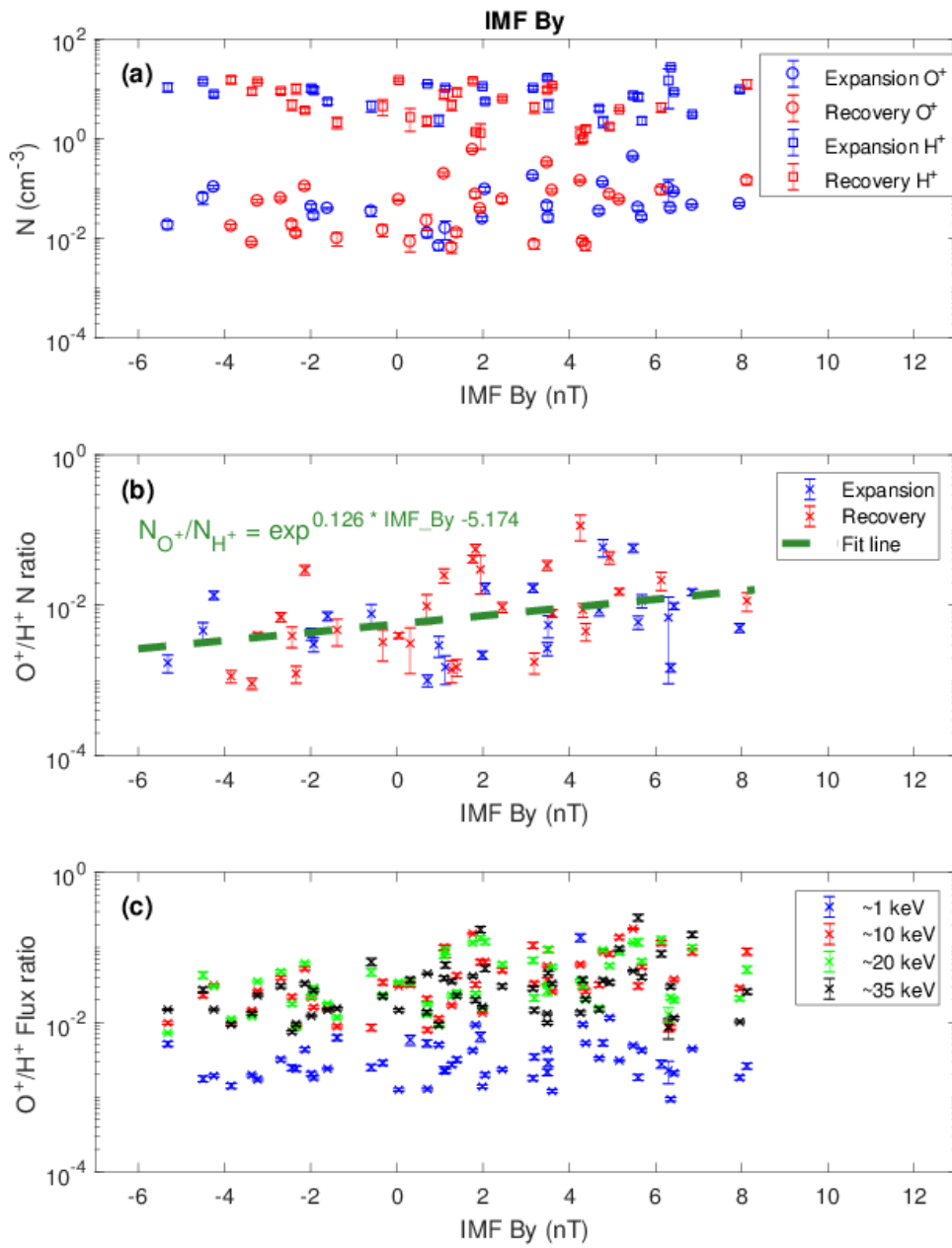
Figure 5. The relationship between the energetic O$^+$ at the duskside magnetopause and IMF By during intense substorms. The format is the same as that of Figure 4.

602

603
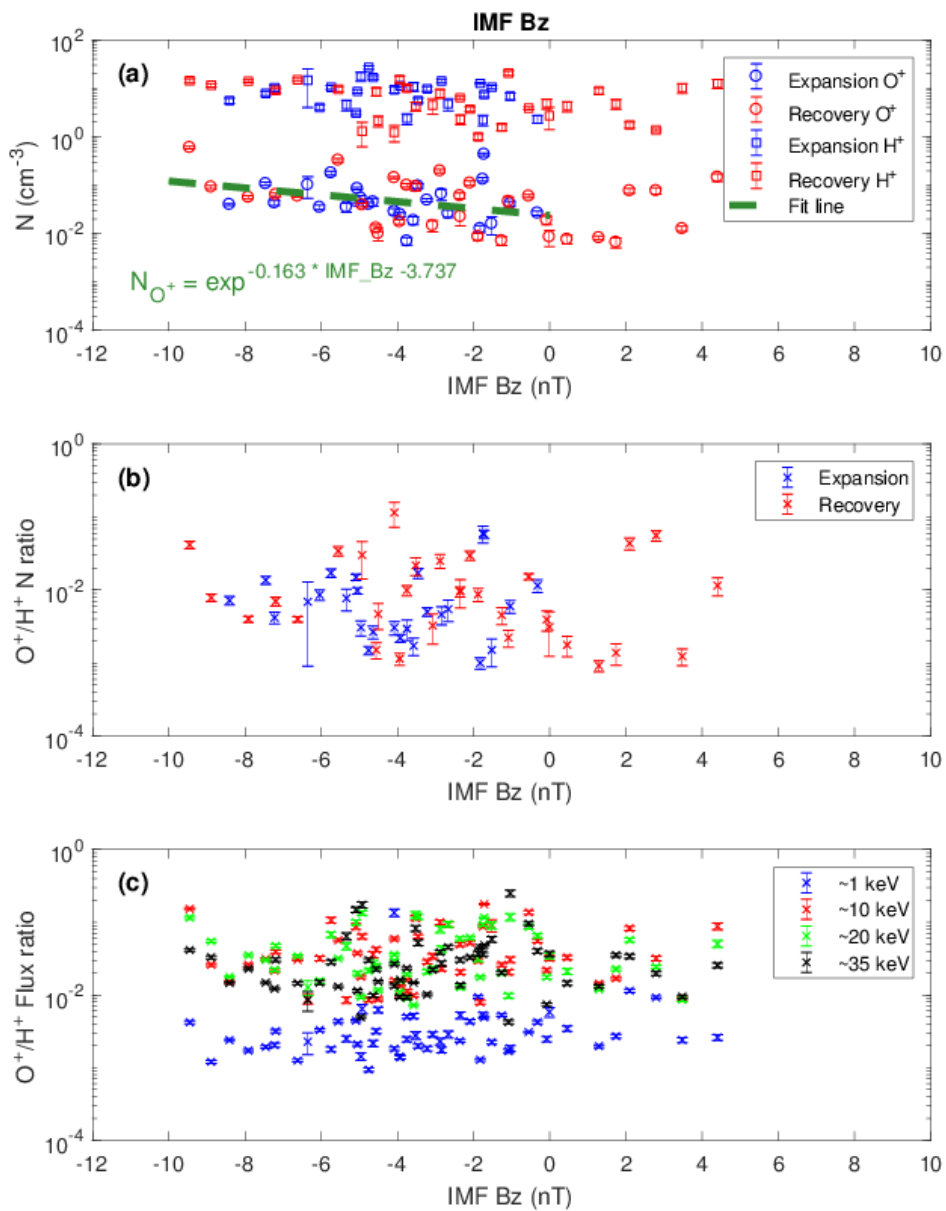
Figure 6. The relationship between the energetic O⁺ at the duskside magnetopause and IMF Bz during intense substorms. The format is the same as that of Figure 4.

606

607
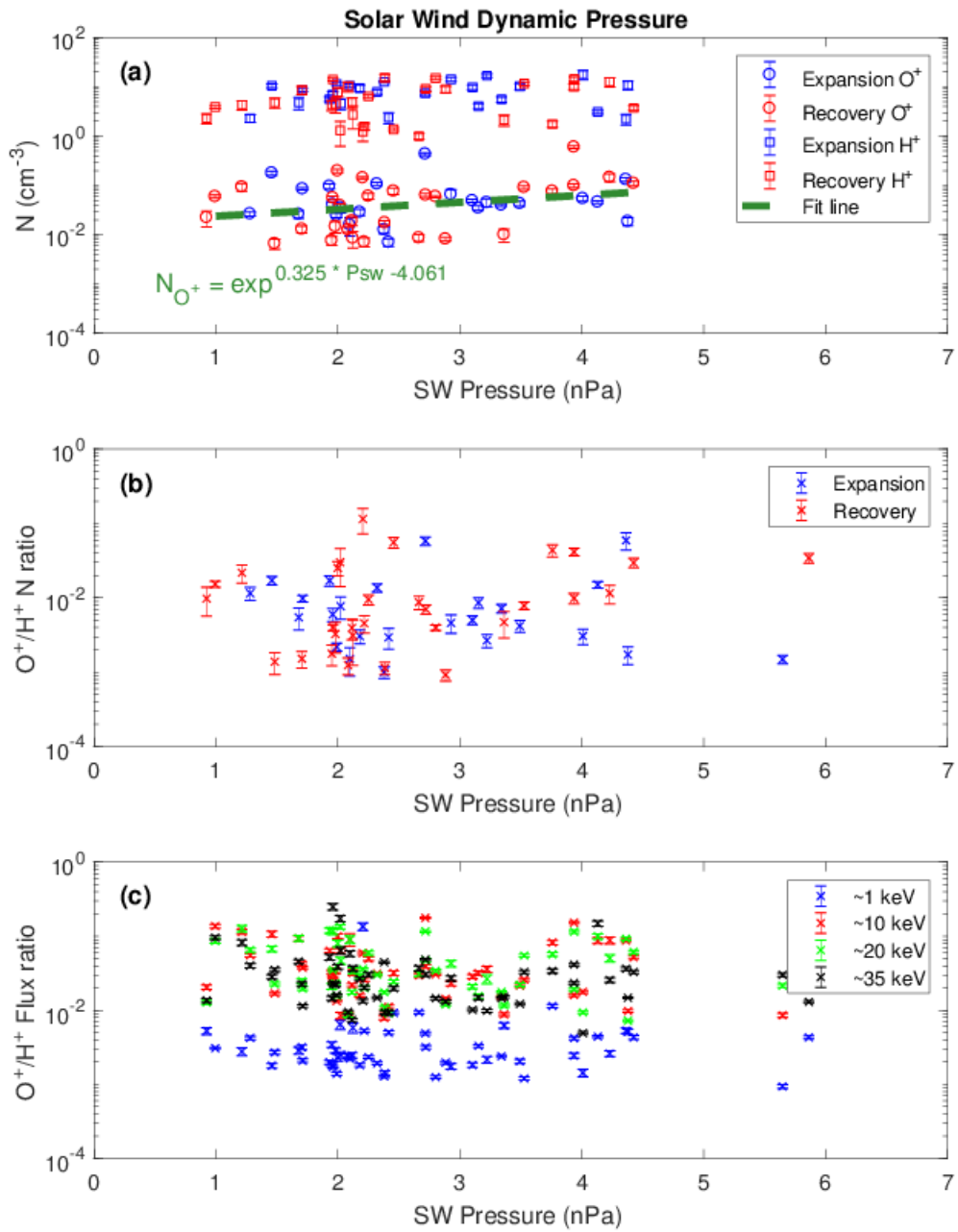
608 **Figure 7.** The relationship between the energetic O^+ at the duskside magnetopause and solar wind
609 dynamic pressure during intense substorms. The format is the same as that of Figure 4.